IEEE Access
Multidisciplinary | Rapid Review | Open Access Journal

Received 4 August 2022, accepted 21 August 2022, date of publication 29 August 2022, date of current version 2 September 2022.

Digital Object Identifier 10.1109/ACCESS.2022.3202536

RESEARCH ARTICLE

A Shape Generation Method for 3D Printed Antennas With Unintuitive Geometries

RYAN J. BENECK, (Student Member, IEEE), GALESTAN MACKERTICH-SENGERDY, (Member, IEEE), SABER SOLTANI, (Senior Member, IEEE), SAWYER D. CAMPBELL, (Senior Member, IEEE), AND DOUGLAS H. WERNER, (Fellow, IEEE)

Department of Electrical Engineering, The Pennsylvania State University, University Park, PA 16802, USA

Corresponding author: Ryan J. Beneck (rbeneck95@gmail.com)

ABSTRACT Additive manufacturing used in combination with versatile shape generation methods can enable designers to realize unintuitive antenna designs with bespoke electromagnetic behaviors that would normally be extremely difficult or even impossible to manufacture using conventional techniques. In this paper, we present a new custom algorithm that produces arbitrary three-dimensional (3D) meander line antennas. This algorithm is used in conjunction with multi-objective optimization to create two quadrifilar helix antennas (QHAs) and one monopole antenna, all with unique electromagnetic performances. One QHA has a wide bandwidth, high broadside gain, and compact size, while the other has a dual-band nature with different radiation patterns in each band. Similarly, the monopole example is a dual-wideband design which targets Wi-Fi applications. These structures possess a meander radius that varies with height as well as conductor thickness that varies along the meander path which allows for improved antenna performance over conventional meander line antennas. An example design was fabricated and tested in order to validate the performance of the optimized virtual antenna model.

INDEX TERMS 3D-printing, additive manufacturing, antennas, dual-band, multi-objective optimization, wideband.

I. INTRODUCTION

All antennas, no matter what their design, have inherent performance constraints based on their geometry [1]. Generally, fewer constraints result in a larger design space which can be exploited to realize antennas with unintuitive and complex geometries that have desirable properties such as wide bandwidth, high gain, strong circular polarization, and compact size [2], [3], [4]. However, some level of constraints are needed as completely unrestricted antennas may not be fabricable with traditional methods such as CNC machining. Fortunately, additive manufacturing techniques such as 3D printing provide a good solution to realizing freeform antenna structures since most structurally stable designs that can be modeled in CAD tools can be 3D printed [5], [6], [7], [8]. However, since the design space for truly three-dimensional antennas is potentially much larger than those using traditional highly constrained methods, new modeling techniques must be used to take full advantage of this increased dimensionality while making optimization of these 3D designs tractable. [9], [10], [11], [12].

Many of these unintuitive geometries are based on the helix antenna, originally introduced by John Kraus in the late 1940s [13], [14] with two primary modes of operation: normal and axial. Helix antennas are widely used for many applications, including global positioning systems, cellular communication [15], weather satellites [16], satellite tracking [17] and television broadcasting [18], but they tend to be limited in bandwidth [19].

Four individual helical antenna elements can be combined to form a quadrifilar helix antenna (QHA). This improves performance in multiple ways such as reduced sidelobes and better axial ratio albeit with increased manufacturing difficulty [20], [21]. One alternative design with improved bandwidth

The associate editor coordinating the review of this manuscript and approving it for publication was Chan Hwang See.

is the conical spiral antenna (CSA). It was invented by John Dyson in the late 1950s and is based on Rumsey's principles of frequency independent antennas [22], [23]. Different sections of the antenna are excited by different frequencies, creating active regions. This allows the structure to operate effectively over a wide frequency range [24], [25], [26]. There are also examples of optimization being employed in the design of these types of antennas [27].

Another important concept in antenna design is tapering [28]. An electromagnetic structure could make use of conductors of varying width to modify its impedance and improve matching. This commonly occurs in the vicinity of the feed or can sometimes be found in the antenna body itself, especially in planar designs [29]. Tapers are usually limited to simple geometries and rarely appear on volumetric wire antennas [30].

A technique for generating freeform helical-like antennas with spatially-varying conductor thickness and arbitrary cross-section could improve the performance of conventional helical antennas while being compatible with state-of-the-art multi-objective optimization procedures. This would enable a straightforward methodology for inverse-design of antennas with complex and unintuitive geometries which meet a set of user-defined performance objectives. To this end, we introduce our approach.

This manuscript presents a new freeform design method for wire antennas that combines properties of QHAs, CSAs, and tapering in order to overcome each of their limitations. As mentioned previously, QHAs traditionally have narrow bandwidth. This can be improved slightly by using multiple concentric helices, but the difference is minor given the increase in complexity [31]. CSAs have better bandwidth but do not typically operate in normal mode and can have asymmetries in their gain pattern. In addition, tapering can be difficult to achieve using traditional subtractive fabrication methods.

Using our method, we can create antennas which have significantly enhanced performance over comparable designs found in the literature. To demonstrate this capability, we realize a compact QHA with over 100% fractional bandwidth. Furthermore, another benefit of our method is the ability to create innovative antennas with disruptive behavior not common in literature, such as a QHA that possesses distinct and tailored radiation patterns in different frequency bands. In addition, to demonstrate that the proposed method is not limited to helix-like geometries, we realize a dual-wideband volumetric monopole for use in Wi-Fi applications. We then demonstrate that such antennas can be 3D printed using Verowhite plastic and then metallized with conductive silver paint [32], [33]. This approach allows for cheap and rapid prototyping.

An overview of the proposed method is shown in Fig. 1. We start by replicating a standard wideband monopole, similar to [34]. Then, we proceed to make various modifications such as changing the base shape, varying the monopole's profile along the height, introducing twisting, and altering

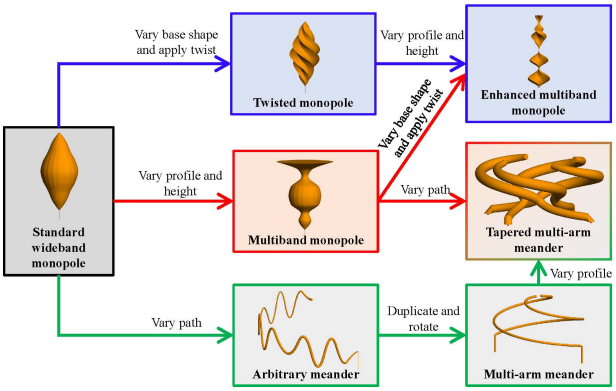

FIGURE 1. Types of antenna geometries possible using our method. Starting with a standard wideband monopole, various types of adjustments can be made to achieve many different results.

the meander path. There is a large potential for disruptive and unintuitive antenna geometries through the use of this method, and the three examples presented in this work only represent a small portion of this new and considerably expanded design space. The remainder of this work is organized as follows: Section 2 outlines the process for designing and evaluating antennas using this method, starting with the definition of an arbitrary meander line and ending with a simulated model of the antenna. Section 3 presents three example designs, which consist of two QHAs and one unconventional monopole. It then discusses how they compare to current work in this area, and demonstrates the benefits of searching for antenna designs that go beyond the constraints of traditional geometries. Section 4 will discuss fabrication and measurement results for one of the example designs. Finally, Section 5 provides a summary and conclusions of the paper.

II. ANTENNA DESIGN

In order to effectively generate and simulate an arbitrability shaped 3D meander with variable cross-sectional area, a new design methodology is required to allow the designer to easily generate geometrically diverse meander-line antennas with only a few parameters. Furthermore, converting the shape into a form that can be imported and simulated with full-wave electromagnetic solvers must be an efficient and straightforward process. Once these steps are in place, then optimization can be applied to discover antenna designs which meet certain user-defined performance criteria. Subsection A discusses the shape generation and simulation methods, while subsection B presents the optimization process.

A. SHAPE GENERATION

The first step of the mesh generation process is to define a meander line in 3D space to serve as the path that the antenna must follow. This can be as simple as a straight line in one direction or could be something more complex such as a helical or a knot structure [35], [36], [37]. The path can be created in any number of ways, such as by manually defining

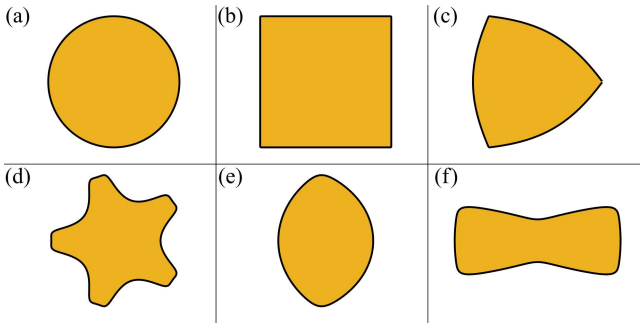

FIGURE 2. Some possible meander cross-sections generated by the superformula [39]. (a) Circle. (b) Square. (c) Reuleaux triangle. (d) Star. (e) Oval. (f) Hourglass.

points, using a parametric curve, or implementing a spline. Then, a "base shape" must be defined, which corresponds to the 2D cross-section of the meander line that follows the 3D path to create the geometry. While a circular cross-section is used as the base shape for the helical designs going forward, any closed planar geometry can be implemented including those based on Bezier or spline surfaces [38] or the superformula [39].

Fig. 2 shows some of the many possible meander cross sections that can be implemented. These include common shapes, such as a circle (Fig. 2(a)) and square (Fig. 2(b)) as well as more unintuitive shapes, such as those in Fig. 2(c) through Fig. 2(f). To the author's knowledge, the ability to generate antenna geometries that are based on an arbitrary 3D meander that also possesses an arbitrary cross section has yet to be reported in the literature.

The next step requires the user to define a number of points and rings which set the element size of the resulting mesh. The number of points specifies how many vertices the base shape contains while the number of rings specifies how many cross-sectional base shapes are created along the 3D path. The shape generator places these cross-sections centered along the meander line and performs a 3D rotation using quaternions to align them with the slope of the line at that point. Each point on a given ring is then connected to two corresponding points on the next ring to create the triangular elements that define the mesh. The total number of mesh triangles is the product of the number of rings and the number of points. Lastly, points are added at start and end of the meander line to serves as caps for the shape and close the mesh. For the studies considered in this paper, we constrained the bottommost ring to be perpendicular to the z-axis to simplify connecting of the antenna feeds.

Fig. 3 displays the main steps involved in mesh creation. An example 3D path which is differentiable at all points is given in Fig. 3(a) while Fig. 3(b) shows the vertices of a mesh which have been generated by rotating and translating a circular base shape according to the position and slope of the line. Fig. 3(c) illustrates how each of the vertices are connected to form a mesh. Each point is connected to the two adjacent ones in the same ring as well as the corresponding point in the next and previous rings. Fig. 3(d) presents the

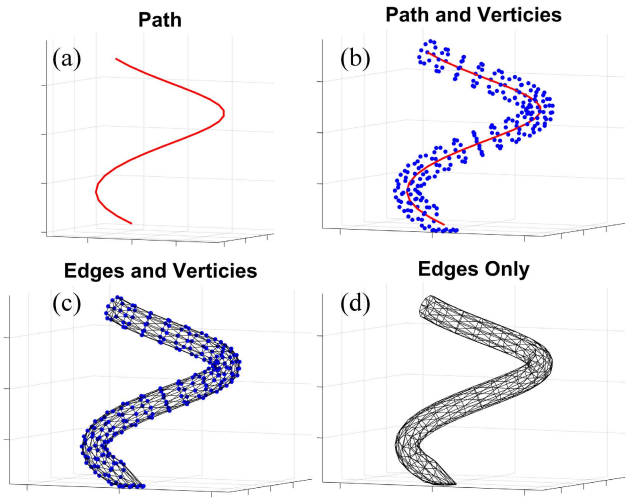

FIGURE 3. Mesh construction technique. Start with a path in 3D space (a). Then create rings centered around the path which are rotated to align with the slope at that point (b). Connect vertices in a systematic fashion to create mesh triangles (c). The mesh triangle data (d) can then be exported to an EM solver.

final mesh without the vertices. Finally, Fig. 4 provides a flowchart describing the mesh generation process.

Once the mesh is created, it can be imported into an electromagnetics simulation tool to assess its performance as an antenna. For the purposes of the studies presented in this paper, FEKO, a commercial method-of-moments (MoM) solver, was chosen for multiple reasons [40]. Firstly, MoM is well suited for analyzing the behavior of a perfect electrical conducting (PEC) body in free space. Secondly, FEKO's built-in scripting language (*i.e.*, EditFEKO) makes it straightforward to import the mesh points and triangle data from the shape generation code. A MATLAB script was created in which the user can input all the necessary parameters to define a geometry. Then it generates an EditFEKO script based on those parameters. It is possible in future work that the shape generation code could be converted to another language such as Python and a different electromagnetic solver package such as HFSS or CST could be utilized.

This method can be further exploited to create designs consisting of more than one meander. In these cases, the shape generator can be run multiple times and a translation or rotation can be applied to each meander. Then, each meander can be individually fed and the properties of each feed, such as input voltage phase and magnitude, can be varied as needed. In the case of a QHA, four separate meanders are generated and then rotated around the z-axis by a 90-degree rotation angle. Note that the relative spacing of each element can be parameterized and tuned during the optimization process. A feed is placed on each arm and the phase of input voltages are offset by $\pi/2$ radians in an order opposed to the helix winding sense. This approach could also be extended further to realize octafilar helical antennas and even designs with an arbitrary number of meanders.

While our shape generation procedure can vary typical parameters such as meander height, radius, and number of

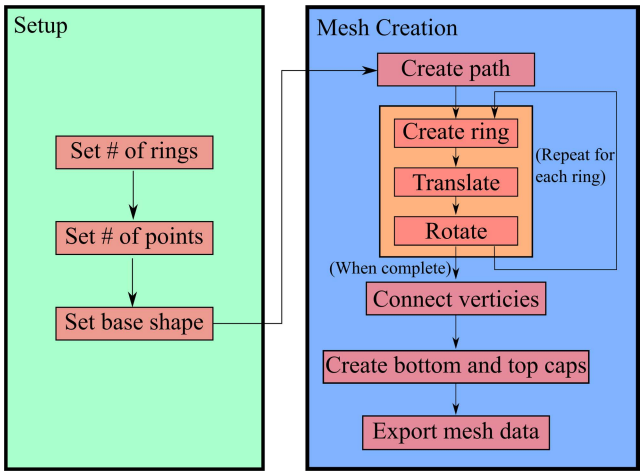

FIGURE 4. Flowchart describing the mesh generation process.

turns, there are many other parameters that can be adjusted. Firstly, the meander radius can vary as a function of height. This allows for a meander whose radial position can vary as a function of the height above the ground plane (or virtual reference surface) while being continuously differentiable at all points. Secondly, the conductor width (*i.e.*, area) of the meander cross-section can be varied along the path of the meander.

$$t = \frac{2\pi n}{h} \tag{1}$$

$$x = \mathrm{r}(z)\sin(t) \tag{2}$$

$$y = \mathrm{r}(z)\cos(t)$$

$$z \in [0, h] \tag{3}$$

For the helical-like antennas discussed in this paper, their meanders can be defined using a simple set of equations. Equation (1) defines the parameter t where h is the height and n is the number of turns. The x and y coordinates are calculated in (2) and (3), respectively, where r(z) is the height dependent meander radius. The z coordinate is bounded between zero and the total height. While only a few parameters are needed to produce geometrically diverse meander antennas, by connecting the shape generation procedure to an appropriate optimization algorithm we can tune the shape parameters in order to realize a custom set of performance criteria.

B. OPTIMIZATION

Multi-objective optimization is a powerful tool for electromagnetic device inverse-design since it can simultaneously minimize the values of multiple competing cost functions (*e.g.*, impedance matching, gain, and other performance metrics) [41]. In this paper, Borg, a multi-objective evolutionary algorithm (MOEA), was chosen due to its ability to self-tune its optimization parameters and robust performance on a wide range of electromagnetics problems [42], [43]. Furthermore, Borg is well suited for parallel processing and can even be run asynchronously for improved multicore performance.

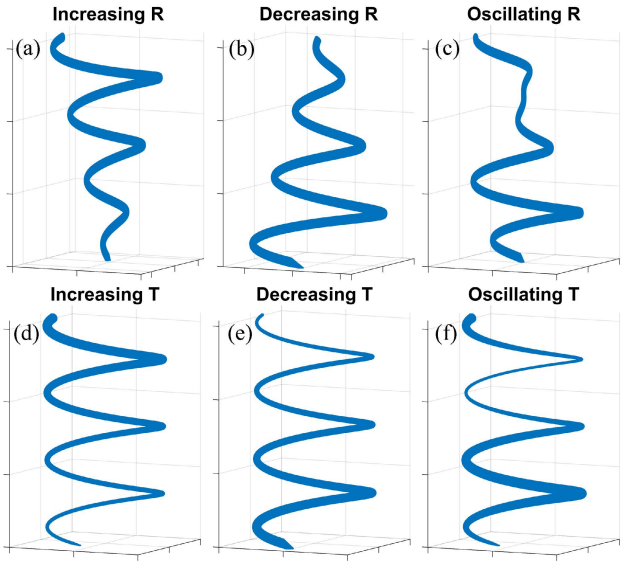

FIGURE 5. Optimization method. Meander radius is made a function of height and can be varied in different ways (a-c). Conductor width is also made a function of height and can be varied in different ways (d-f).

The input parameters for optimization include the meander height, number of turns, N points for meander radius, and M points for conductor width, where N and M can be any positive integer. The points for meander radius are evenly distributed along the height of the structure. They are then fit to a polynomial so the transitions between different radii are smooth. The points for conductor width are distributed in a similar manner, except they are fitted to a spline instead. The values for N and M must be less than or equal to the number of mesh rings. It was found that, for the helix example designs presented later in this work, a value of $N = M = 4$ provided a good balance of optimization time and design space of antenna geometries. With the additional parameters of meander height and number of turns, this results in a total of 10 optimization parameters.

Fig. 5 demonstrates how adjusting optimization parameters can affect the final antenna geometry. For example, inputting an increasing series of values for the meander radius results in a geometry akin to Fig. 5(a), while introducing a decreasing or oscillating series of points produces shapes such as Fig. 5(b) or Fig. 5(c) respectively. In a similar manner, Fig. 5(d), 5(e), and 5(f) portray increasing, decreasing, and oscillating conductor widths respectively. Moreover, designs can have both varying meander radius and varying conductor thickness simultaneously. The minimum meander radius can be zero, which represents a straight wire in the z-direction. However, the conductor width must have a nonzero lower limit or else the antenna would become arbitrarily thin and fabrication would be impractical. The choice of upper limits on each of these parameters are at the designer's discretion, but the max conductor width must be small enough compared to the minimum meander radius as to avoid self-intersection.

III. EXAMPLES

In this section, three example meander antennas were optimized to demonstrate the versatility of the proposed design method. The first example is a dual-band QHA with unique radiation characteristics in each band, the second is a broadband QHA with high gain and over 100% fractional bandwidth, and the third is a dual-wideband monopole for use in Wi-Fi applications. With the dual-band example, our goal was to demonstrate that the proposed method is capable of creating innovative antennas that achieve performance profiles which are not feasible using conventional design techniques. Next, with the broadband example, our goal was to demonstrate that the proposed technique can also be utilized to construct more conventional designs albeit ones that realize enhanced performance over antennas created using traditional methods. Lastly, the monopole example demonstrates the versatility of the method, in that it is not limited to only designing helix-like geometries.

A. DUAL-BAND HELIX

Dual-band QHAs that possess different radiation characteristics in each band typically require a complex mechanical system with moving parts [44] or multiple concentric antennas [32] in order to realize their multi-functionality. Using the method presented in this work, it is possible to create a single antenna with dual-band, dual-mode performance without the need for moving parts. The targeted design is a QHA that exhibits an omnidirectional, linearly polarized gain pattern in one band and a broadside, circularly polarized pattern in the second band. An antenna such as this would be useful in applications where communication to both earth and space-based receivers is desired. For demonstration purposes, the lower band was chosen to be centered at 2 GHz, while the upper was set an octave higher at 4 GHz. However, all dimensions can easily be scaled based on wavelength, so the separation between the two bands as well as the targeted operating frequencies can be chosen arbitrarily. To the author's knowledge, a single QHA with no moving parts and with this performance profile has yet to be presented in the literature.

The following cost functions were utilized to optimize the dual-band QHA

$$cost_1 = S_{11}\,(dB)\,,\ f \in lower \tag{4}$$
$$cost_2 = S_{11}\,(dB)\,,\ f \in upper \tag{5}$$
$$cost_3 = -\text{argmin}\left(G^{\theta=90^\circ}\right),\ f \in lower \tag{6}$$
$$cost_4 = -G^{\theta=0^\circ},\ f \in upper \tag{7}$$
$$cost_5 = height \tag{8}$$

Equations (4) and (5) measure the impedance matching in the lower and upper bands, respectively. Equation (6) concerns the omnidirectionality of the antenna's radiation pattern in the lower band by maximizing the minimum value of the Earth mode gain. Equation (7) seeks to maximize the broadside gain in the upper band. Finally, (8) considers the antenna height with the goal of keeping its footprint small. Note that for (6) and (7), gain values are considered on a linear scale, not dB. In future work, additional cost functions could be implemented to further lessen the antenna's footprint. It could be optimized for properties such as minimal volume and low weight.

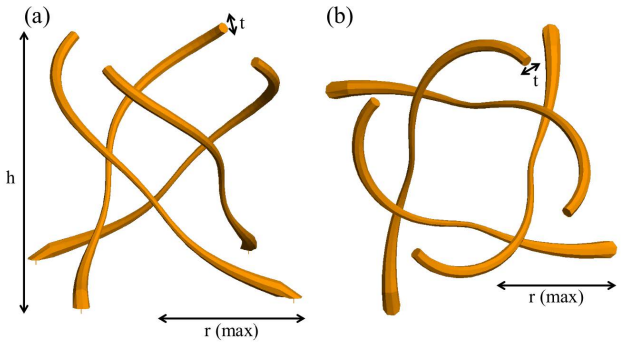

FIGURE 6. Isometric view (a) and top view (b) of dual-band QHA modeled in FEKO.

The lower and upper bounds on the total height are set to 15 mm and 150 mm, respectively. At 4 GHz, this corresponds to a range from 0.2 to 2.0 wavelengths. The number of turns is bounded between 0.5 and 6. The values for conductor width fall between 0.75 mm and 3 mm, which is equivalent to a span from 0.01 to 0.04 wavelengths at 4 GHz. The meander radius was bounded between 6 mm and 75 mm, which corresponds to a range of 0.08 to 1.0 wavelengths in the upper band. Meanwhile, the antenna is fixed to the ground plane with a 1.86 mm gap between the two.

After optimization, a Pareto front of over 100 designs was obtained and a design was selected that met the S_{11} requirement and had the best Earth mode gain, which is the most difficult metric in which to achieve good performance. The selected design has a height of about 70.3 mm with each arm making only half a turn. The meander radius is widest at the base with a value of about 46.7 mm. It then decreases sharply until a quarter of the way up the structure, reaching a minimum radius of 17.7 mm. After that it gradually increases for the remaining height, reaching a value of 32.5 mm at the top. In a similar fashion, the conductor radius is largest at the bottom of the antenna at around 2.7 mm. It then decreases to around 1.4 mm partway up the height and gradually grows for the remaining distance, reaching a final value of 2 mm. The FEKO model showing the geometry of this example antenna is provided in Fig. 6 and a plot of the S_{11} versus frequency is shown in Fig. 7.

Moreover, the far-field patterns in each band are also simulated. At 2 GHz, the QHA operates in normal mode with an omnidirectional radiation pattern. At 4 GHz, the antenna operates in axial mode with a broadside radiation pattern. The maximum gains in the lower and upper bands are 5.9 dB and 10.3 dB respectively. A polar plot of the far-field patterns is shown in Fig. 8. As one can see, the optimizer was able to tune the antenna geometry in order to produce the two desired and distinctly different radiation patterns. The unique performance profile of this antenna is most likely

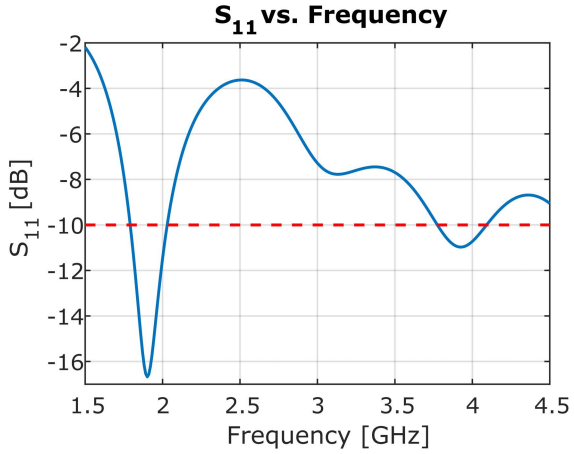

FIGURE 7. S_{11} versus frequency for dual-band QHA.

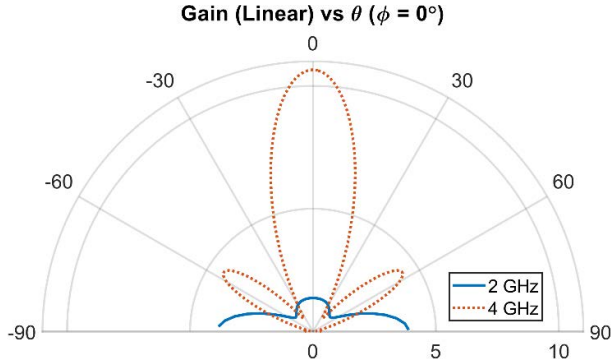

FIGURE 8. Simulated gain of dual-band QHA in both space and earth mode generated using FEKO. At 2 GHz, the radiation pattern is omnidirectional. At 4 GHz, the radiation pattern is unidirectional in the broadside direction.

due to its similarity to conical spiral antennas. It exploits the properties of active regions which come from Rumsey's angle and truncation principles [22], [24]. The tapering also further improves the impedance matching.

B. BROADBAND HELIX

While the goal of the previous example was to create a new type of QHA, our method can also be used to address the existing limitations of more conventional designs. While QHAs commonly suffer from narrow bandwidths, the introduction of a spatially varying meander radius and conductor width can significantly improve their performance in this regard. Thus, the goal for the second example is to optimize an arbitrary QHA that achieves the highest possible bandwidth.

Four different cost functions are used to optimize the geometry of this antenna:

$$cost_1 = \text{argmax}(S_{11}\,(dB)),\ f \in band \tag{9}$$

$$cost_2 = -\text{argmin}\left(G^{\theta=0^\circ}\right),\ f \in band \tag{10}$$

$$cost_3 = \left[\text{argmax}\left(G^{\theta=0^\circ}\right) - \text{argmin}\left(G^{\theta=0^\circ}\right)\right],\ f \in band \tag{11}$$

$$cost_4 = height \tag{12}$$

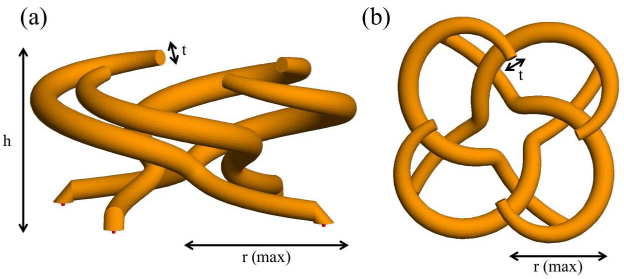

FIGURE 9. Isometric view (a) and top view (b) of broadband QHA modeled using FEKO.

Equation (9) accounts for the bandwidth, which takes the worst S_{11} value over the entire bandwidth and attempts to minimize it. Equation (10) evaluates for the minimum broadside gain over the bandwidth. Equation (11) is the gain span and minimizes the difference between the highest and lowest gain to enable more consistent performance. Equation (12) is meant to minimize the footprint of the antenna. Note that for costs 2 and 3, gain values are considered on a linear scale, not dB. The bounds on all the parameters are identical to the previous example design. However, the gap between the antenna and ground plane was adjusted to a value of 1.24 mm. This gap was smaller than in the dual-band design because it was scaled according to the center frequency of operation. Note that, similar to the dual-band design, additional cost functions could be added to minimize properties such as overall antenna volume and weight.

After optimization, several hundred Pareto optimal designs were found. A design was selected that demonstrated a good balance of wide bandwidth, high gain, and short height while also keeping the difference between the highest and lowest gains small. The FEKO model of this example antenna is shown in Fig. 9 with labels for height, conductor width, and meander radius. The antenna height is only 28 mm, which corresponds to about $\lambda/2$ at the center frequency, giving the antenna a small footprint.

Similar to the dual-band design, each arm makes a little over half a turn. In terms of other parameters, the meander radius is widest at the base with a value of 32.1 mm. It then oscillates between low and high values, reaching a minimum radius of 9.24 mm and ending at a radius of 19.8 mm at the top. The conductor radius gradually increases from 2.4 mm to 2.9 mm along the height, before decreasing to 2 mm once reaching the top.

The simulation results show that the antenna is able to obtain an S_{11} of less than -10 dB over nearly the entire band from 2 GHz to 7 GHz (Fig. 10(a)). This corresponds to a fractional bandwidth of 111% which is higher than what conventional QHAs can normally achieve. Meanwhile, the antenna maintains a maximum gain value between 8 and 10 dB over the entire frequency range of interest (Fig. 10(b)). Similar to the dual-band example, the design of this antenna exploits properties of active regions to achieve a wide bandwidth, and its tapered arms further improve impedance matching.

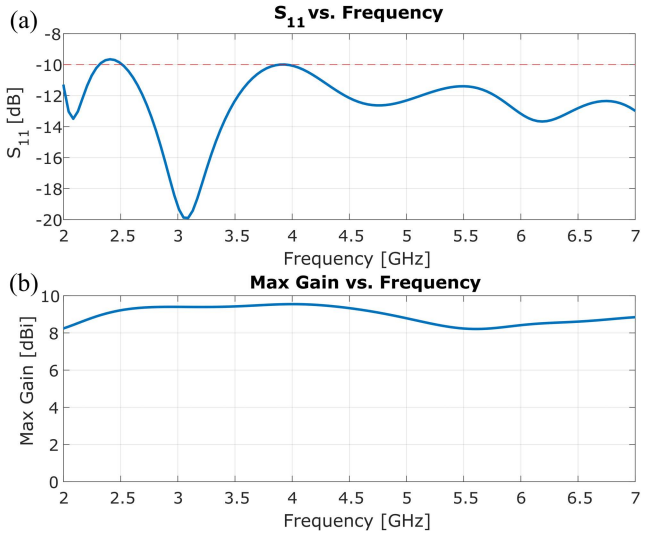

FIGURE 10. Simulated broadband QHA performance metrics. (a) S_{11} versus frequency. (b) Maximum gain versus frequency.

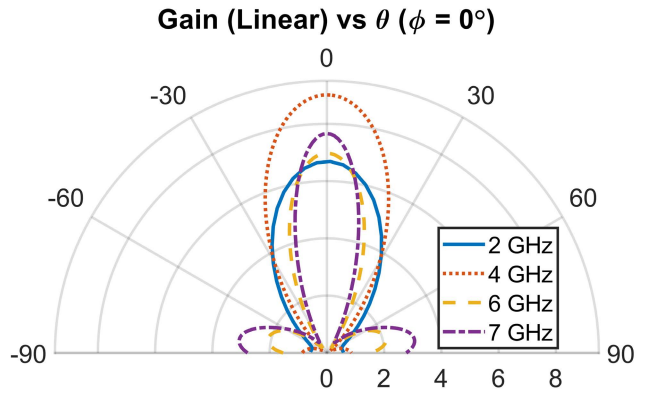

FIGURE 11. Simulated gain of broadband QHA over multiple frequencies.

The far-field gain pattern was then calculated and is presented in Fig. 11. One can see that the antenna forms a stable broadside beam over the entire frequency range. Moreover, the gain is entirely left-hand circularly polarized (LHCP) with no coupling to the orthogonal polarization.

The antenna maintains a good S_{11} from 2 GHz to 7 GHz, which corresponds to a fractional bandwidth of 111%. Additionally, in order to demonstrate the benefits of the taper, a separate simulation was performed. A duplicate of this antenna was created in FEKO but with the same conductor width along the entire antenna structure. It is observed in Fig. 12 that the taper significantly improves impedance matching in the middle of the frequency band. Also, note that the antenna was simulated using an infinite ground plane to decrease the required computational time. However, additional tests were performed which demonstrated that a 10 cm ground plane was sufficient in minimizing any effects on performance. Compared to similar antennas in the literature, this antenna surpasses most previous designs in terms of fractional bandwidth and gain, while remaining comparable in terms of size (see Table 1). While the design presented

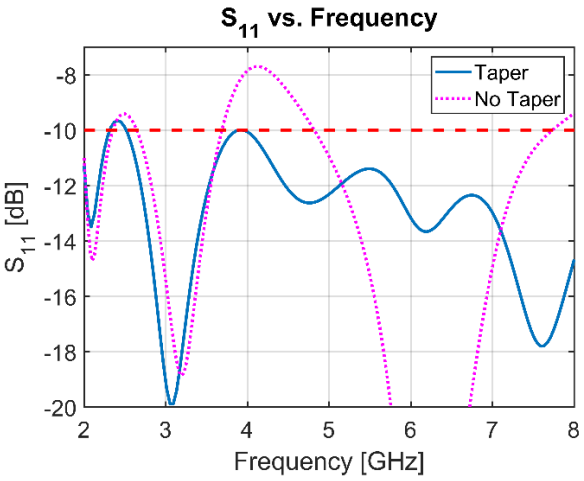

FIGURE 12. Analysis of taper effects. A tapered meander results in enhanced S_{11} performance compared to a constant conductor width.

TABLE 1. Comparison to similar desings in the literature.

Design	Frequency Range	FBW	Height (H/λ center)	Gain (dBi)	Fabricated
[45]	1.14-2.47 GHz	73.1 %	1.08	5-10.5	Yes
[46]	8-12 GHz	40 %	0.65	7.6	No
[47]	1.19-2.5 GHz	71 %	1.4268	~4.25	No
[48]	2-2.2 GHz	9.5 %	1.47	3.7	Yes
[49]	1.6 – 5.96 GHz	116 %	3.75	6-13.2	Yes
This work	2-7 GHz	111 %	0.524	8.2-9.54	Yes

in [49] achieves similar performance to our design, it requires a much larger footprint.

C. WI-FI MONOPOLE

While the previous examples have focused on QHAs, the proposed method is not limited to this type of geometry. In fact, it is trivial to restrict the meander path to be a straight line along the z-axis and proceed to vary the meander width, twisting, and base shape to create geometrically diverse monopole-type antennas. Our goal here is to create a multi-band 3D monopole which operates over different Wi-Fi regimes.

This antenna targets the frequencies of 2.4 GHz and 6 GHz to make it applicable for present and future Wi-Fi applications [50]. In total, 13 design parameters were used including 9 values defining the meander width along the height, and values which govern the monopole height, offset above the ground plane, amount of twisting, and a selection of one of six base shapes (Fig. 2). The following four cost functions were employed:

$$cost_1 = \text{argmax}(S_{11}\,(dB)),\ f \in band \tag{13}$$

$$cost_2 = \text{argmax}\,(|S_{11}\,(dB)|)\,,\ f \notin band \tag{14}$$

$$cost_3 = -\text{argmin}\Big(\text{argmin}\left(G^{\theta=90^\circ}_{f=2.4GHz}\right), \text{argmin}\left(G^{\theta=90^\circ}_{f=2.5GHz}\right)\Big) \tag{15}$$

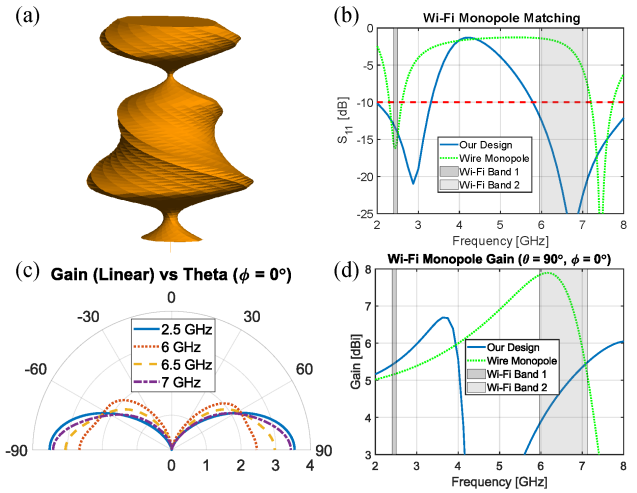

FIGURE 13. Summary of simulated FEKO results of the dual-wideband Wi-Fi monopole on an infinite ground. (a) Antenna geometry. (b) S_{11} vs. frequency results compared to a wire monopole of the same size. (c) Radiation patterns for various frequencies in the Wi-Fi bands. (d) Omnidirectional gainvs. frequency results compared to a wire monopole of the same size.

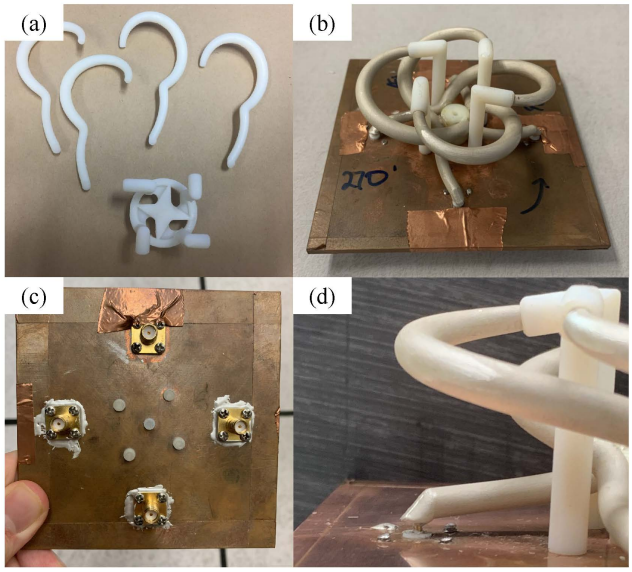

FIGURE 14. (a) Printed antenna arms and mount. (b) Metallized antenna mounted on copper ground plane. (c) Underside of antenna with connectors. (d) Close up view of connection to antenna arm.

$$cost_4 = -\text{argmin}\Big(\text{argmin}\left(G^{\theta=90^\circ}_{f=6GHz}\right), \text{argmin}\left(G^{\theta=90^\circ}_{f=6.5GHz}\right), \text{argmin}\left(G^{\theta=90^\circ}_{f=7.1GHz}\right)\Big)$$

Equation (13) attempts to achieve a good match in each of the two target bands. Next, (14) makes sure the antenna maintains a multi-band property by forcing poor matching at frequencies which are out of band. Lastly, (15) and (16) attempt to improve the omnidirectional gain within the lower and upper bands, respectively. Potential future studies could add additional cost functions which would aim to reduce the volume and weight of the antenna for further reduced footprint.

After optimization, a Pareto front of about 100 designs was generated, and one design was selected that provided a good balance of each of the performance goals. Fig. 13(a) shows the selected antenna's geometry which is modeled in FEKO. Fig. 13(b) presents the S_{11} behavior as a function of frequency and compares it to a traditional quarter-wave wire monopole. Fig. 13(c) shows the omnidirectional radiation patterns over various in-band frequencies. Note that these patterns are entirely vertically polarized. Lastly, Fig. 13(d) compares the peak gain of our design to a quarter-wave monopole over various frequencies. The final design's tapered structure with narrow and wide sections contributes to its dual-wideband nature.

While there exist examples of dual-band monopoles in the literature; however, to the author's knowledge, they are either planar [51], [52] or have relatively narrow bandwidth in each band [53]. In addition, this antenna is able to achieve good performance over common Wi-Fi bands without the need for a matching network and while maintaining the same size as a conventional quarter-wave monopole.

IV. EXPERIMENTAL DEMONSTRATION

The broadband QHA example design was selected as a good candidate for fabrication and testing in order to validate the efficacy of the proposed design approach. A mount was designed in Solidworks to provide mechanical support for the antenna during operation and was produced using a Stratasys Objet260 Connex3 3D printer and VeroWhite plastic. The mount was designed to provide mechanical rigidity for the structure while having minimal impact on the electromagnetic performance.

Next, high resolution 3D models of each QHA arm were exported from FEKO as.stl files so as to be compatible with the 3D printer system. Since each arm is identical, four copies of one arm were printed. Once printed, each VeroWhite arm was sprayed with conductive silver paint and a 0.065-inch bit was used to drill a hole into the bottom of each to facilitate easy connection to the feeds. The antenna was assembled on the mount and attached to a square 10 cm copper ground plane with four holes. SMA connectors were placed on the underside of the ground so as to pass through it and slot into the holes in each antenna arm. This allows each arm to be fed individually while adding a minimal amount of conductive material above the ground plane that might interfere with performance.

The conductivity of the silver paint is 8.3 x 10^5 S/m. Through an additional Feko study, its radiation efficiency was found to be approximately 99% over the frequency band. Therefore, the metallization process is not expected to have any significant detrimental effects on performance for this design.

The steps for antenna fabrication are highlighted in Fig. 14. The printed antenna arms and the mount prior to metallization are displayed in Fig. 14(a), while Fig. 14(b) shows the metallized antenna and mount attached to the copper ground plane.

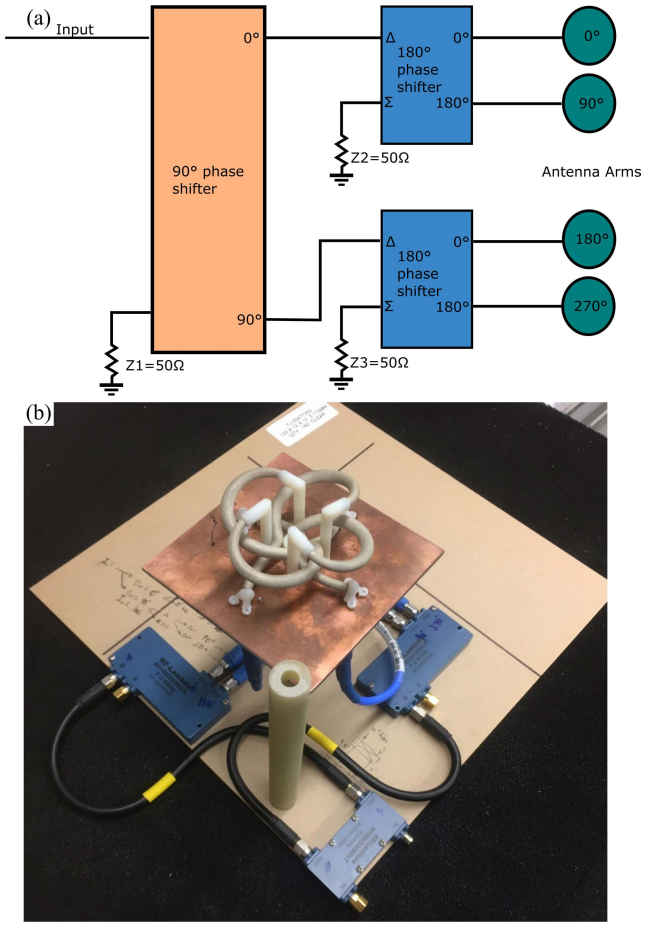

FIGURE 15. (a) Diagram of feeding network. (b) Fully assembled antenna with feeding network mounted to a copper-clad FR4 plate.

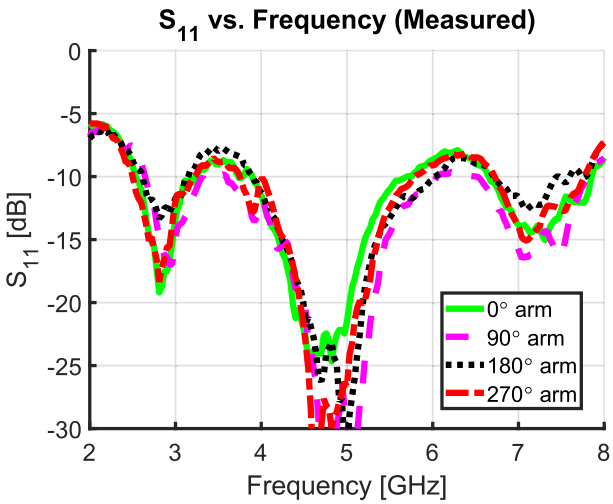

FIGURE 16. Measured S_{11} versus frequency for each arm of the QHA.

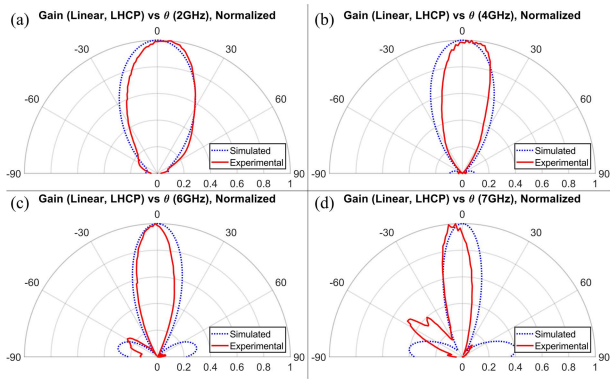

FIGURE 17. Comparison of simulated and measured normalized LHCP gain. A constant 6-degree offset was added to the measured data to account for chamber misalignment. (a) 2 GHz. (b) 4 GHz. (c) 6 GHz. (d) 7 GHz.

Copper tape is added over the screws to prevent them having any negative impact on the performance. An image of the underside of the antenna setup with the connectors passing through the ground plane is given in Fig. 14(c). Finally, Fig. 14(d) shows a close-up of how the port and the antenna are connected.

In order for this QHA to operate properly, the phase of the input voltage on each arm must be offset with phases of 0, 90, 180, and 270 degrees and arranged in such a fashion where the direction of increasing phase opposes the helix winding sense. To ensure performance is maintained over the entire bandwidth, the phase difference between the four arms must be held constant. This can be achieved using a wideband feeding network built from commercially available phase shifters [54]. We note that future alterations of the design could make use of a more compact custom feeding network [55]. The feeding network consists of two 180-degree hybrid phase shifters and one 90-degree hybrid phase shifter, which are all rated for operation between 2 GHz to 8 GHz. The specific models in use were purchased from RF-Lambda and include the RFHB02G08GPI coaxial 30W 180-degree hybrid and the RFHB02G08GVT coaxial 50W 90-degree hybrid coupler respectively. Both are lightweight and compact.

A diagram of the phase shifter arrangement is illustrated in Fig. 15(a). A single input is connected to the 90-degree phase shifter. Then each output from that component connects to the input of one of the 180-degree phase shifters. Finally, each output of the 180-degree phase shifter connects to each antenna arm oriented counter to the helix winding sense. The isolated ports on every component are connected to 50-Ohm load.

The phase shifters are placed on a copper-clad FR4 plate underneath the antenna and ground plane. SCA49240-12 and RFC6969A-E9NL305 cables were used to connect the components. A FR4 dowel rod is also mounted on the base plate to support the antenna and the ground plane. The entire setup with the base plate, phase shifters, dowel, cables, ground plane, mount, and antenna is shown in Fig. 15(b).

The antenna and ground plane system was measured using a vector network analyzer by connecting each port to a different VNA input. The resulting S_{11} versus frequency plot for each antenna arm is shown in Fig. 16. The measured results indicate good impedance matching, with the S_{11} being less than -10 dB over most of the band. Also, each of the four QHA arms have near identical performance, which

is expected based on the simulated results. However, there is reduced performance at low frequencies around 2.0 to 2.5 GHz, which is most likely a result of minor fabrication inaccuracies.

The antenna was then measured in an anechoic chamber. Fig. 17 shows the normalized measured LHCP far-field patterns compared to the simulation case at four different frequencies. The normalized patterns are offset by a constant of 6 degrees. This is most likely a result of misalignment when mounting in the chamber. After adjusting, the experimental data matches well to the simulated results.

V. CONCLUSION

The ability to easily model freeform 3D meanders with arbitrary cross-sections and varying conductor thicknesses represents a new paradigm in antenna design methodology. Utilizing this new method in combination with 3D printing technology allows for the fabrication of a variety of new and unintuitive antenna configurations. In addition, meanders designed using this technique are defined by a small number of parameters and can be easily optimized for any arbitrary criteria using powerful multi-objective techniques. The three examples showcased here were a dual-band QHA with different radiation characteristics in each band, a wideband high-gain QHA, and a dual-wideband monopole. The wideband QHA outperforms similar designs in literature and has applications in areas such as global positioning, cellular communication, and radio astronomy. While the dual-band antenna could potentially be used in a situation which would usually require two separate antennas or a complex system involving moving parts. Lastly, the monopole example is capable of being employed in current and future Wi-Fi systems as well as demonstrates that the method introduced here is not limited to helix-like geometries. Fabrication is straightforward and inexpensive with feeding networks that can be easily constructed using commercially available phase shifters. Measured results for the broadband QHA compare favorably to simulations. Finally, the designs shown in this paper are only three examples, and the proposed design procedure is capable of producing a multitude of other complex structures with unique and disruptive behaviors.

ACKNOWLEDGMENT

The authors thank Ronald P. Jenkins and Ryan J. Chaky for their suggestions and advice related to the project.

REFERENCES

[1] C. A. Balanis, "Antenna theory: A review," *Proc. IEEE*, vol. 80, no. 1, pp. 7–23, Jan. 1992, doi: 10.1109/5.119564.

[2] B. Mishra, R. K. Verma, N. Yashwanth, and R. K. Singh, "A review on microstrip patch antenna parameters of different geometry and bandwidth enhancement techniques," *Int. J. Microw. Wireless Technol.*, vol. 14, no. 5, pp. 652–673, 2022, doi: 10.1017/S1759078721001148.

[3] R. Cicchetti, E. Miozzi, and O. Testa, "Wideband and UWB antennas for wireless applications: A comprehensive review," *Int. J. Antennas Propag.*, vol. 2017, pp. 1–45, Feb. 2017, doi: 10.1155/2017/2390808.

[4] E. Altinozen, I. Harrison, A. Vukovic, and P. Sewell, "Systematic generation of arbitrary antenna geometries," *IEEE Trans. Antennas Propag.*, early access, Apr. 13, 2022, doi: 10.1109/TAP.2022.3165539.

[5] N. R. Famularo, L. Kang, Z. Li, T. Zhao, K. L. Knappenberger, C. D. Keating, and D. H. Werner, "Linear and nonlinear chiroptical response from individual 3D printed plasmonic and dielectric microhelices," *J. Chem. Phys.*, vol. 153, no. 15, Oct. 2020, Art. no. 154702, doi: 10.1063/5.0020539.

[6] M. D. Gregory, J. A. Easum, and D. H. Werner, "A wideband axially symmetric antenna design fabricated with additive and subtractive methods," in *Proc. IEEE Int. Symp. Antennas Propag. (APSURSI)*, Fajardo, PR, USA, Jun. 2016, pp. 813–814, doi: 10.1109/APS.2016.7696115.

[7] R. J. Beneck and D. H. Werner, "Design of unintuitive antenna geometries using additive manufacturing techniques," in *Proc. IEEE Int. Symp. Antennas Propag. North Amer. Radio Sci. Meeting*, Montreal, QC, Canada, Jul. 2020, pp. 1311–1312, doi: 10.1109/IEEECONF35879.2020.9330170.

[8] S. Wang, F. Fan, Y. Xu, Z.-C. Guo, W. Zheng, Y.-T. Liu, and Y. Li, "3-D printed zirconia ceramic Archimedean spiral antenna: Theory and performance in comparison with its metal counterpart," *IEEE Antennas Wireless Propag. Lett.*, vol. 21, no. 6, pp. 1173–1177, Jun. 2022, doi: 10.1109/LAWP.2022.3161004.

[9] D. Z. Zhu, P. L. Werner, and D. H. Werner, "Design and optimization of 3-D frequency-selective surfaces based on a multiobjective lazy ant colony optimization algorithm," *IEEE Trans. Antennas Propag.*, vol. 65, no. 12, pp. 7137–7149, Dec. 2017, doi: 10.1109/TAP.2017.2766660.

[10] D. Z. Zhu, E. B. Whiting, S. D. Campbell, D. B. Burckel, and D. H. Werner, "Optimal high efficiency 3D plasmonic metasurface elements revealed by lazy ants," *ACS Photon.*, vol. 6, no. 11, pp. 2741–2748, Nov. 2019, doi: 10.1021/acsphotonics.9b00717.

[11] D. Z. Zhu, M. D. Gregory, P. L. Werner, and D. H. Werner, "Fabrication and characterization of multiband polarization independent 3-D-printed frequency selective structures with ultrawide fields of view," *IEEE Trans. Antennas Propag.*, vol. 66, no. 11, pp. 6096–6105, Nov. 2018, doi: 10.1109/TAP.2018.2866507.

[12] V. Basile, M. Grande, V. Marrocco, D. Laneve, S. Petrignani, F. Prudenzano, and I. Fassi, "Design and manufacturing of supershaped dielectric resonator antennas for 5G applications using stereolithography," *IEEE Access*, vol. 8, pp. 82929–82937, 2020, doi: 10.1109/ACCESS.2020.2991358.

[13] J. D. Kraus, "Helical beam antennas for wide-band applications," *Proc. IRE*, vol. 36, no. 10, pp. 1236–1242, Oct. 1948, doi: 10.1109/JRPROC.1948.231603.

[14] J. D. Kraus, "The helical antenna," *Proc. IRE*, vol. 37, no. 3, pp. 263–272, Mar. 1949, doi: 10.1109/JRPROC.1949.231279.

[15] G. Zhou and B. Yildirim, "A multi-band fixed cellular phone antenna," in *IEEE Antennas Propag. Soc. Int. Symp. Dig. Held Conjunct USNC/URSI Nat. Radio Sci. Meeting*, vol. 1, Orlando, FL, USA, Jul. 1999, pp. 112–115, doi: 10.1109/APS.1999.789095.

[16] A. Gupta and S. R. Chopra, "Designing and testing of quadrifilar helix antenna for NOAA weather satellite," in *Proc. 6th Int. Conf. Signal Process. Integr. Netw. (SPIN)*, Noida, India, Mar. 2019, pp. 785–790, doi: 10.1109/SPIN.2019.8711572.

[17] V. Laquerbe and R. Fragnier, "Metallic S-band antenna for satellite TT&C links," *IEEE Antennas Wireless Propag. Lett.*, vol. 21, no. 4, pp. 715–719, Apr. 2022, doi: 10.1109/LAWP.2022.3143769.

[18] F. M. Zeki and A. H. M. Al-Dalawie, "Design and implementation a non-uniform helical antenna in frequency range of 450–850 MHz for ultra-high-frequency television application," *Cihan Univ., Erbil Sci. J.*, vol. 3, no. 2, pp. 75–79, Aug. 2019, doi: 10.24086/cuesj.v3n2y2019.pp75-79.

[19] J. M. Tranquilla and S. R. Best, "A study of the quadrifilar helix antenna for global positioning system (GPS) applications," *IEEE Trans. Antennas Propag.*, vol. 38, no. 10, pp. 1545–1550, Oct. 1990.

[20] B. Slade, "The basics of quadrifilar helix antennas," RF Globalnet Newslett., Orlando, FL, USA, Tech. Rep., 2015. [Online]. Available: https://www.rfglobalnet.com/doc/the-basics-of-quadrifilar-helix-antennas-0001

[21] H. Wang, Y. Zhang, S. Chen, Y. Ma, H. Wang, Y. Chen, and X. Feng, "Mechanics design of conical spiral structure for flexible coilable antenna array," *Int. J. Aerosp. Eng.*, vol. 2022, pp. 1–8, May 2022, doi: 10.1155/2022/4265384.

[22] V. Rumsey, "Frequency independent antennas," in *Proc. IRE Int. Conv. Rec.*, vol. 5, New York, NY, USA, 1957, pp. 114–118, doi: 10.1109/IRECON.1957.1150565.

[23] J. Dyson, "The unidirectional equiangular spiral antenna," *IRE Trans. Antennas Propag.*, vol. 7, no. 4, pp. 329–334, Oct. 1959, doi: 10.1109/TAP.1959.1144707.

[24] T. W. Hertel and G. S. Smith, "Analysis and design of two-arm conical spiral antennas," *IEEE Trans. Electromagn. Compat.*, vol. 44, no. 1, pp. 25–37, Feb. 2002, doi: 10.1109/15.990708.

[25] T. W. Hertel and G. S. Smith, "The conical spiral antenna over the ground," *IEEE Trans. Antennas Propag.*, vol. 50, no. 12, pp. 1668–1675, Dec. 2002, doi: 10.1109/TAP.2002.807429.

[26] A. Gu, S. Yang, and Z. Nie, "Analysis and design of miniaturized ultra-wideband conical log spiral antennas," in *Proc. Cross Strait Quad-Regional Radio Sci. Wireless Technol. Conf.*, Chengdu, China, Jul. 2013, pp. 191–194, doi: 10.1109/CSQRWC.2013.6657385.

[27] M. Chetioui, A. Boudkhil, M. Damou, and N. Benahmed, "A new conical helix antenna based on MEMS technology using genetic algorithms," in *Proc. 6th Int. Conf. Image Signal Process. Their Appl. (ISPA)*, Mostaganem, Algeria, Nov. 2019, pp. 1–6, doi: 10.1109/ISPA48434.2019.8966852.

[28] R. W. Klopfenstein, "A transmission line taper of improved design," *Proc. IRE*, vol. 44, no. 1, pp. 31–35, Jan. 1956, doi: 10.1109/JRPROC.1956.274847.

[29] V. N. R. Vanukuru, "Low insertion-loss stacked transformers using tapered spirals for high performance RFICs," in *Proc. IEEE 19th Top. Meeting Silicon Monolithic Integr. Circuits RF Syst. (SiRF)*, Orlando, FL, USA, Jan. 2019, pp. 1–3, doi: 10.1109/SIRF.2019.8709044.

[30] B. Ning, J. Lei, Y. Cao, and L. Dong, "A conical quadrifilar helix antenna for GNSS applications," in *Proc. Int. Symp. Antennas Propag.*, 2013, pp. 543–546.

[31] W. A. Shah, S. Shoaib, Q. Islam, and M. Amin, "Wide band side fed bifilar helix antenna caged in passive quadrifilar helix structure," in *Proc. IEEE Radio Wireless Symp. (RWS)*, New Orleans, LA, USA, Jan. 2010, pp. 597–600, doi: 10.1109/RWS.2010.5434217.

[32] S. Shoaib, W. A. Shah, M. Amin, and N. Shoaib, "Dual mode helix antenna for wideband terrestrial and GPS L2 communications," in *Proc. 5th Eur. Conf. Antennas Propag. (EUCAP)*, 2011, pp. 233–236.

[33] V. Kyovtorov, I. Georgiev, S. Margenov, D. Stoychev, F. Oliveri, and D. Tarchi, "New antenna design approach—3D polymer printing and metallization. Experimental test at 14–18 GHz," *AEU, Int. J. Electron. Commun.*, vol. 73, pp. 119–128, Mar. 2017, doi: 10.1016/j.aeue.2016.12.017.

[34] M. H. Gandomi and D. Zarifi, "Design and development of ultra-wideband 3-D monopole antennas based on supercurves," *IEEE Trans. Antennas Propag.*, vol. 69, no. 12, pp. 8214–8220, Dec. 2021, doi: 10.1109/TAP.2021.3090832.

[35] W. Mai, L. Kang, R. Jenkins, D. Zhu, C. Mao, P. L. Werner, Y. Chen, and D. H. Werner, "A knotted metamolecule with axisymmetric strong optical activity," *Adv. Opt. Mater.*, vol. 8, no. 23, Dec. 2020, Art. no. 2000948, doi: 10.1002/adom.202000948.

[36] D. H. Werner, D. M. Jones, and P. L. Werner, "The electromagnetic fields of elliptical torus knots," *IEEE Trans. Antennas Propag.*, vol. 49, no. 6, pp. 980–991, Jun. 2001, doi: 10.1109/8.931157.

[37] S. V. Kumar and A. R. Harish, "Generation of circularly polarized conical beam pattern using torus knot antenna," *IEEE Trans. Antennas Propag.*, vol. 65, no. 11, pp. 5740–5746, Nov. 2017, doi: 10.1109/TAP.2017.2754403.

[38] E. B. Whiting, S. D. Campbell, G. Mackertich-Sengerdy, and D. H. Werner, "Dielectric resonator antenna geometry-dependent performance tradeoffs," *IEEE Open J. Antennas Propag.*, vol. 2, pp. 14–21, 2021, doi: 10.1109/OJAP.2020.3037826.

[39] J. Gielis, "A generic geometric transformation that unifies a wide range of natural and abstract shapes," *Amer. J. Botany*, vol. 90, no. 3, pp. 333–338, Mar. 2003, doi: 10.3732/ajb.90.3.333.

[40] E. Almajali, D. McNamara, and D. Lee, "Using electromagnetic simulation code FEKO as a numerical laboratory in antenna engineering," in *Proc. 14th Int. Symp. Antenna Technol. Appl. Electromagn. Amer. Electromagn. Conf.*, Ottawa, ON, Canada, Jul. 2010, pp. 1–4, doi: 10.1109/ANTEM.2010.5552545.

[41] S. H. Yeung, W. S. Chan, K. T. Ng, and K. F. Man, "Computational optimization algorithms for antennas and RF/microwave circuit designs: An overview," *IEEE Trans. Ind. Informat.*, vol. 8, no. 2, pp. 216–227, May 2012, doi: 10.1109/TII.2012.2186821.

[42] J. Nagar and D. H. Werner, "A comparison of three uniquely different state of the art and two classical multiobjective optimization algorithms as applied to electromagnetics," *IEEE Trans. Antennas Propag.*, vol. 65, no. 3, pp. 1267–1280, Mar. 2017.

[43] D. Hadka and P. Reed, "Borg: An auto-adaptive many-objective evolutionary computing framework," *Evol. Comput.*, vol. 21, no. 2, pp. 231–259, May 2013, doi: 10.1162/EVCO_a_00075.

[44] M. Amin, R. Cahill, and V. F. Fusco, "Mechanically tunable multiband compact quadrifilar helix antenna with dual mode operation," *IEEE Trans. Antennas Propag.*, vol. 56, no. 6, pp. 1528–1532, Jun. 2008, doi: 10.1109/TAP.2008.923331.

[45] Z. Ren, S.-S. Qi, Z. Hu, Z. Shen, and W. Wu, "Wideband water helical antenna of circular polarization," *IEEE Trans. Antennas Propag.*, vol. 67, no. 11, pp. 6770–6777, Nov. 2019, doi: 10.1109/TAP.2019.2922846.

[46] S. He, H. Wang, Y. Wang, S. Quan, and D. Xu, "A helix antenna with broad beamwidth for wideband applications," in *Proc. 12th Int. Symp. Antennas, Propag. EM Theory (ISAPE)*, Hangzhou, China, Dec. 2018, pp. 1–3, doi: 10.1109/ISAPE.2018.8634239.

[47] C. Wu, M. He, and C. Zhang, "A wideband and low-unroundness printed conical equiangular-spiral antenna," in *Proc. 6th Asia–Pacific Conf. Antennas Propag. (APCAP)*, Oct. 2017, pp. 1–3, doi: 10.1109/APCAP.2017.8420996.

[48] M. Taherkhani, J. Tayebpour, S. Radiom, and H. Aliakbarian, "Circularly polarised wideband quadrifilar helix antenna with ultra-wide beamwidth isoflux pattern for a S-band satellite ground station," *IET Microw., Antennas Propag.*, vol. 13, no. 10, pp. 1699–1704, Aug. 2019.

[49] X. Liu, C. L. Zekios, and S. V. Georgakopoulos, "Analysis of a packable and tunable origami multi-radii helical antenna," *IEEE Access*, vol. 7, pp. 13003–13014, 2019, doi: 10.1109/ACCESS.2019.2892711.

[50] *IEEE Standard for Information Technology—Telecommunications and Information Exchange Between Systems—Local and Metropolitan Area Networks—Specific Requirements—Part 11: Wireless LAN Medium Access Control (MAC) and Physical Layer (PHY) Specifications*, IEEE Standard 802.11-2020 (Revision of IEEE Standard 802.11-2016), Feb. 2021, pp. 1–4379, doi: 10.1109/IEEESTD.2021.9363693.

[51] M.-T. Tan and B.-Z. Wang, "A dual-band circularly polarized planar monopole antenna for WLAN/Wi-Fi applications," *IEEE Antennas Wireless Propag. Lett.*, vol. 15, pp. 670–673, 2016, doi: 10.1109/LAWP.2015.2466596.

[52] N. K. Sahu and S. K. Mishra, "Compact dual-band dual-polarized monopole antennas using via-free metasurfaces for off-body communications," *IEEE Antennas Wireless Propag. Lett.*, vol. 21, no. 7, pp. 1358–1362, Jul. 2022, doi: 10.1109/LAWP.2022.3167849.

[53] W. Tan and Z. Shen, "A dual-band dual-sleeve monopole antenna," *IEEE Antennas Wireless Propag. Lett.*, vol. 16, pp. 2951–2954, 2017, doi: 10.1109/LAWP.2017.2755042.

[54] H. R. Fang, M. Serhir, R. Balakrishnan, R. Guinvarc'h, and K. Mouthaan, "Low profile cavity-backed four-arm Archimedean spiral antenna with 8:1 bandwidth," in *Proc. 8th Eur. Conf. Antennas Propag. (EuCAP)*, The Hague, Netherlands, Apr. 2014, pp. 2528–2531, doi: 10.1109/EuCAP.2014.6902333.

[55] Y.-P. Lyu, L. Zhu, and C.-H. Cheng, "Single-layer broadband phase shifter using multimode resonator and shunt λ/4 stubs," *IEEE Trans. Compon., Packag., Manuf. Technol.*, vol. 7, no. 7, pp. 1119–1125, Jul. 2017, doi: 10.1109/TCPMT.2017.2691739.

RYAN J. BENECK (Student Member, IEEE) received the B.S. degree in electrical engineering from the University of Delaware, Newark, DE, USA, in 2018. He is currently pursuing the Ph.D. degree in electrical engineering with the Penn State University, University Park, PA, USA.

Since 2018, he has been a Research Assistant with the Computational Electromagnetics and Antennas Research Laboratory, Penn State University. His research interests include antenna design and metamaterials.

GALESTAN MACKERTICH-SENGERDY (Member, IEEE) received the B.S. degree in mechanical engineering and the M.S. degree in engineering science and mechanics from Penn State University, University Park, PA, USA, where he is currently pursuing the Ph.D. degree in electrical engineering.

From 2009 to 2018, he worked in industry as a Mechanical Engineer. Since 2019, he has been a Researcher with the Computational Electromagnetics and Antennas Research Laboratory, Penn State University. His research interests include designing mechanically robust, high-power, metamaterial antenna systems.

SABER SOLTANI (Senior Member, IEEE) received the B.E. degree, in 2006, the M.Phil. degree from Urmia University, Iran, in 2008, and the Ph.D. degree from The Hong Kong University of Science and Technology (HKUST), in 2016, all in electrical and communication engineering.

From 2009 to 2012, he worked as a Senior Researcher and a Lecturer at Urmia University. His postdoctoral research experience includes HKUST, in 2016, and the University of Massachusetts Boston/Lowell, from 2017 to 2018. He is currently a Postdoctoral Fellow with the Computational Electromagnetics and Antennas Research Laboratory (CEARL), Department of Electrical Engineering, The Pennsylvania State University. His research interests include MIMO antenna design and optimization, high impedance surface design (HIS), transmission line modeling (TLM), RF device design and their application for wireless communication, and biomedical applications.

Dr. Soltani was a recipient of the CST University Publication Award, in 2015, the HKUST Overseas Research Award to visit The University of Arizona, in 2016, and the Honorable Mention Paper Awards from the IEEE International Symposium on Antennas and Propagation/USNC–URSI National Radio Science meeting (IEEE APS/URSI) in 2015, 2016, and 2017.

SAWYER D. CAMPBELL (Senior Member, IEEE) received the B.S. degree in physics from Illinois Wesleyan University, Bloomington, IL, USA, in 2008, and the M.S. and Ph.D. degrees in optical sciences from The University of Arizona, Tucson, AZ, USA, in 2010 and 2013, respectively.

He was an Undergraduate Researcher with the Intense Laser Physics Theory Unit, Department of Physics, Illinois State University, from 2004 to 2008. He was then a Graduate Research Associate with the La Casa de Creative Electromagneticists, Department of Electrical and Computer Engineering, The University of Arizona, under the advisement of Prof. Richard W. Ziolkowski. In 2014, he joined the Computational Electromagnetics and Antennas Research Laboratory, Department of Electrical Engineering, The Pennsylvania State University, as a Postdoctoral Scholar, under the advisement of Prof. Douglas H. Werner. Since 2022, he has been an Associate Research Professor with the Department of Electrical Engineering, Penn State University, and is also the Associate Director of the Computational Electromagnetics and Antennas Research Laboratory (CEARL). He has extensive experience in the computational modeling and inverse-design of metamaterial- and transformation optics-based devices at RF, infrared, and optical frequencies. Additionally, he is an expert in the application of multiobjective and surrogate-assisted optimization techniques to challenging problems in both the RF and optical regimes. He has published over 100 technical papers and proceedings articles, co-edited a book on nanoantennas and plasmonics, and is the author/coauthor of five book chapters. His current research interests include metasurfaces, plasmonics, geometrical optics, gradient-index lenses, transformation optics high power microwave antennas, optimization, and applications of deep learning to RF and optical inverse-design problems.

Dr. Campbell is a member of OPTICA and SPIE and is the past Chair and the Current Vice-Chair/Treasurer of the IEEE Central Pennsylvania Section.

DOUGLAS H. WERNER (Fellow, IEEE) received the B.S. and M.S. degrees in electrical engineering, the M.A. degree in mathematics, and the Ph.D. degree in electrical engineering from The Pennsylvania State University (Penn State), University Park, in 1983, 1985, 1986, and 1989, respectively.

He holds the John L. and Genevieve H. McCain Chair Professorship with the Department of Electrical Engineering, Pennsylvania State University. He is the Director of the Computational Electromagnetics and Antennas Research Laboratory (CEARL: http://cearl.ee.psu.edu/) as well as a Faculty Member of the Materials Research Institute (MRI: https://www.mri.psu.edu/) at Penn State. He holds 20 patents, has published over 980 technical papers and proceedings articles, and 30 book chapters with several additional chapters (currently in preparation). He has published seven books, including *Frontiers in Electromagnetics* (Piscataway, NJ, USA: IEEE Press, 2000), *Genetic Algorithms in Electromagnetics* (Hoboken, NJ, USA: Wiley-IEEE Press, 2007), *Transformation Electromagnetics and Metamaterials: Fundamental Principles and Applications* (London, U.K.: Springer, 2014), *Electromagnetics of Body Area Networks: Antennas, Propagation, and RF Systems* (Hoboken, NJ, USA: Wiley/IEEE, 2016), *Broadband Metamaterials in Electromagnetics: Technology and Applications* (London, U.K.: Taylor & Francis Group, 2017), *Nanoantennas and Plasmonics: Modelling, Design and Fabrication* (London, U.K.: SciTech Publishing, IET, 2020), and *Electromagnetic Vortices: Wave Phenomena and Engineering Applications* (Hoboken, NJ, USA: Wiley-IEEE Press, 2021). He has also contributed chapters for several books, including *Electromagnetic Optimization by Genetic Algorithms* (New York: Wiley Interscience, 1999), *Soft Computing in Communications* (New York: Springer, 2004), *Antenna Engineering Handbook* (New York: McGraw-Hill, 2007), *Frontiers in Antennas: Next Generation Design and Engineering* (New York: McGraw-Hill, 2011), *Numerical Methods for Metamaterial Design* (New York: Springer, 2013), *Computational Electromagnetics* (New York: Springer, 2014), *Graphene Science Handbook: Nanostructure and Atomic Arrangement* (Abingdon, Oxfordshire, U.K.: CRC Press, 2016), *Handbook of Antenna Technologies* (New York: Springer, 2016), and *Transformation Wave Physics: Electromagnetics, Elastodynamics, and Thermodynamics* (Boca Raton, FL: CRC Press, 2016). His research interests include computational electromagnetics (MoM, FEM, FEBI, FDTD, DGTD, CBFM, RCWA, GO, and GTD/UTD) antenna theory and design, phased arrays (including ultra-wideband arrays), microwave devices, wireless and personal communication systems (including on-body networks), wearable and e-textile antennas, RFID tag antennas, conformal antennas, reconfigurable antennas, frequency selective surfaces, electromagnetic wave interactions with complex media, metamaterials, electromagnetic bandgap materials, zero and negative index materials, transformation optics, nanoscale electromagnetics (including nanoantennas), fractal and knot electrodynamics, and nature-inspired optimization techniques (genetic algorithms, clonal selection algorithms, particle swarm, wind driven optimization, and various other evolutionary programming schemes).

Prof. Werner is a fellow of IET, OPTICA, SPIE, ACES, and the PIER Electromagnetics Academy. He is also a Senior Member of the National Academy of Inventors (NAI) and the International Union of Radio Science (URSI). He is also a member of URSI Commissions B and G, Eta Kappa Nu, Tau Beta Pi, and Sigma Xi. He was presented with the 1993 Applied Computational Electromagnetics Society (ACES) Best Paper Award and was also the recipient of the 1993 International Union of Radio Science (URSI) Young Scientist Award. In 1994, he received the Pennsylvania State University Applied Research Laboratory Outstanding Publication Award. He was the coauthor (with one of his graduate students) of a paper published in the IEEE TRANSACTIONS ON ANTENNAS AND PROPAGATION which received the 2006 R. W. P. King Award. He received the IEEE Antennas and Propagation Society Edward E. Altshuler Prize Paper Award and the Harold A. Wheeler Applications Prize Paper Award, in 2011 and 2014, respectively. In 2018, he received the DoD Ordnance Technology Consortium (DOTC) Outstanding Technical Achievement Award. He also received the 2015 ACES Technical Achievement Award, the 2019 ACES Computational Electromagnetics Award, and the IEEE Antennas and Propagation Society 2019 Chen-To Tai Distinguished Educator Award. He was a recipient of a College of Engineering PSES Outstanding Research Award and Outstanding Teaching Award, in March 2000 and March 2002, respectively. He was also presented with an IEEE Central Pennsylvania Section Millennium Medal. In March 2009, he received the PSES Premier Research Award. He is a former Associate Editor of *Radio Science*, a former Editor of the *IEEE Antennas and Propagation Magazine*, a former Editorial Board Member of *Scientific Reports* (a Nature subjournal), an Editorial Board Member of *EPJ Applied Metamaterials*, and an Editor of the IEEE PRESS SERIES ON ELECTROMAGNETIC WAVE THEORY AND APPLICATIONS.